Escola de Primavera de Transição e Turbulência
Blumenau 2022

ABCM
13th Spring School on Transition and Turbulence
September 19th-23rd, 2022, Blumenau, SC, Brazil

EPTT-2022-0076
A droplet-based image velocimetry technique for the measurement of liquid velocity fields in two-phase water-oil dispersion flows

Rafael Franklin Lázaro de Cerqueira
William Monte Verde
Jorge Luiz Biazussi
Center for Petroleum Studies, University of Campinas, Cora Coralina Street, 350, Campinas, São Paulo, Brazil
rafaelfc@unicamp.br, wmv@unicamp.br, jorge.biazussi@gmail.com
Rodolfo Marcilli Perissinotto
Marcelo Souza de Castro
Antonio Carlos Bannwart
School of Mechanical Engineering, University of Campinas, Mendeleyev Street, 200, Campinas, São Paulo, Brazil
rodolfomp@fem.unicamp.br, mscastro@unicamp.br, bannwart@unicamp.br

Abstract. *The present work describes a measurement technique to estimate the continuous liquid velocity fields in two-phase water-oil dispersion flows. A transparent pump prototype made of acrylic was firstly developed and installed to enable the use of flow visualization and optical measurement techniques. Then, in the experiments, water droplets were injected into the impeller channels of the centrifugal pump, where a mineral oil with a viscosity of μ_o = 18.0 cP was used as the continuous phase. The two-phase water-oil dispersion flow was then filmed with a high-speed camera, and the water droplets were black-dyed for a better contrast with the white background. When injecting the water drops, breakage events were frequently observed due to turbulence and shear effects, resulting in the birth of small droplets with a size in the range from 100 μm to 500 μm. The occurrence of small water droplets in combination with the viscous continuous oil phase meant that those droplets could be assumed as tracer particles from the continuous phase. Therefore, by computing the small water droplet velocities, it is possible to estimate the velocity field of the continuous oil phase within an acceptable error margin. This is the main idea of the technique presented in this work, which does not require the addition of intrusive tracer particles, and thus can be seen as a cheap and simple alternative to PIV in two-phase dispersions with continuous viscous phases. After a series of image processing steps, the small water droplets in the range from 100 μm to 500 μm are identified, and the PTV technique computes their instantaneous velocity. In order to assess the method capabilities, the PTV ensemble-averaged liquid flow rate is compared against experimental values from a Coriolis flowmeter installed in the experimental setup. The technique is then applied to study the flow within a pump impeller, resulting in similar flow patterns found in the literature for studies using LDV and PIV studies.*

Keywords: *Centrifugal pump, PTV, Droplets, Water-oil dispersion flows*

1. INTRODUCTION

Centrifugal pumps are widely used as an artificial lift method in the oil industry. In general, those pumps are designed to operate with low viscous fluids and in single-phase flow conditions (Gülich, 2008). However, during operation in oil fields, the pumps must operate in out of design conditions, such as two-phase flows where gas is present (Monte Verde *et al.*, 2017) in the pipeline or with viscous fluids (Monte Verde *et al.*, 2013), which may be due to the viscosity of the continuous phase or product of an emulsion (Bulgarelli *et al.*, 2021). In these cases, the pump performance decays, leading to unstable operations and even premature equipment failure. Due to the widespread use of centrifugal pumps by the oil industry and the typical harsh conditions faced in oil fields, several studies are dedicated to a better understanding of the pump performance degradation in these unfavourable conditions.

These studies concern the evaluation of the pump performance over global parameters, such as the modification of pump performance curves due to the presence of the gas-phase (Monte Verde *et al.*, 2017), viscous fluids (Monte Verde *et al.*, 2013) or due to unstable emulsions (Bulgarelli *et al.*, 2021). For two-phase flows, it is possible to design a transparent pump prototype and film the phase distribution through high-speed camera imaging. This approach was adopted in Zhang *et al.* (2016); Monte Verde *et al.* (2017); Zhao *et al.* (2021); Stel *et al.* (2019) for the visualization of gas-liquid flow inside the pump impeller channels and for analyzing the drop dynamics in liquid-liquid flows, as in Perissinotto *et al.* (2019, 2020). Some of these works even attempted to track the dispersed phase's motion to generate averaged or instantaneous results for better comprehension of the flow within the pump impeller. That was the case for Perissinotto *et al.* (2019), which manually tracked oil drops in oil-in-water dispersed flow, and Perissinotto *et al.* (2020) which employed the same manual tracking technique for water-in-oil dispersed in cases where the water-droplets were well-defined in high-speed camera images. The same approach was used in Stel *et al.* (2019) to study the bubble dynamics in a gas-liquid two-phase flow in a centrifugal pump impeller.

Recently, in de Cerqueira *et al.* (2021) and de Cerqueira *et al.* (2022), the authors of the present work developed a

fully automated Particle Tracking Velocimetry (PTV) technique to track the motion of dispersed oil drops within centrifugal pump impellers. Compared to the manual tracking approach, the use of an automatic PTV technique results in a large number of tracked dispersed drops, which, when time or ensemble-averaged, can result in average fields that can fully describe the dispersed phase dynamics, resulting in a better comprehension of the two-phase flow within the pump impellers.

In single-phase flows, the Particle Image Velocimetry (PIV) technique can be used to characterize the continuous phases, returning the velocity field within the pump geometry (Keller *et al.*, 2014; Li *et al.*, 2020; Liu *et al.*, 2021). In the past two decades, several studies employing the PIV technique were published to better understand the pump performance in single-phase flows, as described in the detailed review of Perissinotto *et al.* (2021). The drawback of the PIV technique is the requirement of a fully transparent test section, which also requires a geometry that enables a planar illumination lighting setup. In the oil industry, the centrifugal pump stages usually have complex geometries, such as vaned diffusers (Monte Verde *et al.*, 2017), which imposes difficulties on the use of the PIV technique due to planar illumination requirement. For this reason, most of the PIV studies on centrifugal pump impellers published so far are limited to simple geometries. The same argument is valid for the application of the PIV technique in multiphase flows since the presence of an additional phase may obstruct the illumination sheet, impeding the use of the experimental technique or requiring the use of additional image processing techniques (Cerqueira *et al.*, 2018). In addition, as described in Perissinotto *et al.* (2021), despite the common occurrence of viscous fluid in the oil industry, the PIV technique has not been applied to investigate the flow within centrifugal pumps operating in such conditions.

The same difficulties reported above are typical when using the PIV technique in bubbly flows. Recently, to overcome those difficulties and estimate the liquid velocity field in a bubble column, Ziegenhein *et al.* (2016) describe a technique based on the tracking capabilities of microbubbles, which naturally occur in bubbly flows. Due to their small size, the authors assumed that the microbubbles acted as tracer particles. By controlling the camera depth of field and the focus plane, the authors could compare their technique against results obtained with planar PIV acquisitions, resulting in good agreement. Therefore, the technique can be seen as a cheap and simple alternative to the PIV technique for certain two-phase systems and phase arrangements.

In the present work, a similar strategy as the one described in Ziegenhein *et al.* (2016) is used to estimate the oil continuous velocity field in two-phase flow water-in-oil dispersions from the high-speed camera images from Perissinotto *et al.* (2020). In their work, independent of the pump operations conditions, small dispersed water droplets naturally occur within the pump impeller channels. Thus, image processing steps are employed to identify and classify the small water droplets according to their size. Then, the PTV technique is used to compute the instantaneous velocity of the micrometre-sized droplets, which with the assumptions detailed in the current work, represent the velocity of the continuous, viscous oil phase. The method is assessed by calculating the oil flow rate against experimentally measured values from a Coriolis flowmeter and used to analyze the flow within a centrifugal pump impeller.

2. EXPERIMENTAL SETUP

Experiments were performed in the experimental setup described in Perissinotto *et al.* (2020). The apparatus is composed of a oil flow-line and an water injection system, in addition to a centrifugal pump prototype based on a real pump model commonly used in oil wells. In order to visualize the flow inside the impeller channels, the top shroud was removed and replaced by a transparent one. This modification allowed the study of gas-liquid flows in Monte Verde *et al.* (2017) and liquid-liquid flows in Perissinotto *et al.* (2019) and Perissinotto *et al.* (2020). The schematic diagram of the experimental facility is shown in Fig. 1.

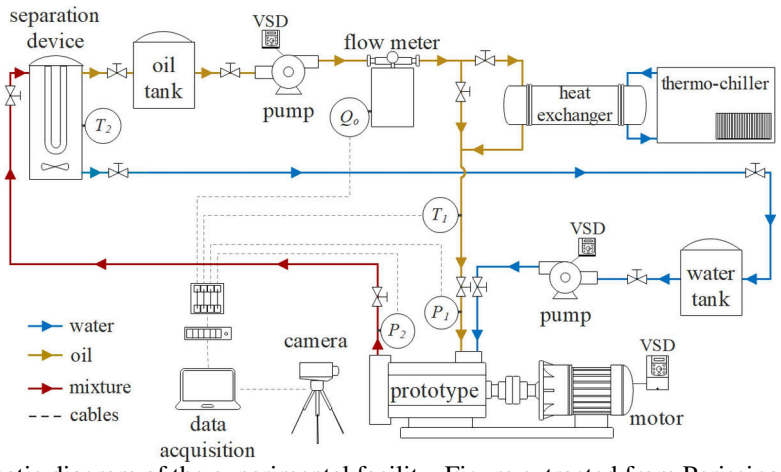

Figure 1: Schematic diagram of the experimental facility. Figure extracted from Perissinotto *et al.* (2020).

The experimental facility comprises two separate fluid lines, one for the continuous oil phase and a second for the dispersed water drops. The oil phase flow rate is controlled by a booster pump, connected to a variable speed drive and a control valve. Before entering the prototype test section, a Coriolis flowmeter measures the oil flow rate (Q_o). A peristaltic pump injects the water drops into the impeller channels. For better control, the peristaltic pump operates with a constant injection rate Q_w = 0.0072 m^3/h (around 2 ml/s). A handheld tachometer measures the pump prototype impeller speed (N). The outlet (P_2) and inlet pressures (P_1) are measured by capacitive transducers. The transparent pump prototype has an inner and outer impeller radius of, respectively, $R_{min} = 22$ mm and $R_{max} = 55$ mm, while the the channel height, which corresponds to the distance between the transparent window and the impeller bottom is h = 6 mm.

By injecting the two phases, a water-in-oil dispersion is observed within the pump impeller channels. The continuous oil phase is mineral oil with a density (ρ_o) of 838 kg/m^3 and viscosity (μ_o) of 0.018 Pa s (18 cP) at a temperature of 25 ^{o}C, and oil/water interfacial tension ($\sigma_{o/w}$) of 24 mN/m. The temperature of the oil phase is held constant by the thermo-chiller and heat exchanger, which keeps the oil phase at a constant temperature of 25 ^{o}C. In order to enhance the water drop contrast against the white background, the water phase is dyed with methylene blue. This does not alters the water phase properties, resulting in a density (ρ_o) of 998 kg/m^3 and viscosity (μ_o) of 0.00090 Pa s (0.9 cP) at a temperature of 25 ^{o}C.

The article by Perissinotto *et al.* (2020) contains a detailed description of all devices present in the experimental facility.

2.1 Experimental Matrix

The high-speed videos used in the present work were taken from Perissinotto *et al.* (2020), filmed with a *Phantom VEO 640*, with a resolution of 2560x1600 pixels at a 2000 fps acquisition rate. The experimental matrix, comprised of 3 experimental flow conditions, is shown in Tab. 1, with a single pump rotational speed and three different oil flow rates. Around 3000 and 5000 frames were acquired during each footage, corresponding of a filming time of 1.5 s and 2.5 s. Therefore, during the acquisitions the pump impeller completed a total of around 15 and 25 full rotations.

Table 1: High-speed camera videos used in the present work and originally presented in Perissinotto *et al.* (2020). In all experiments the dispersed water drops were injected with a constant flow rate of Q_w = 0.0072 m^3/h.

Experiment	N [rpm]	Q_o [m^3/h]	$\dot{m}_o$ [kg/h]	BEP
1	600	0.97	812.86	0.8 Q_{BEP}
2		1.21	1013.98	1.0 Q_{BEP}
3		1.45	1215.10	1.2 Q_{BEP}

The oil flow rates are listed in Tab. 1 as multiples of the pump's best efficiency point (BEP). Regarding the pump prototype performance curves, the injection of the water droplets into the impeller pump channels did not alter the performance curves. Therefore, it is assumed that the water drops do not affect the flow within the impeller pump channels. For more details, the reader may address to Perissinotto *et al.* (2020).

As discussed by Perissinotto *et al.* (2020), the water drop size and shape present a complex morphology, depending on the continuous phase flow rate and pump impeller rotation. After entering the impeller channel, the water drops are elongated and deformed by the action of the surrounding continuous oil flow. As the elongated water drops become thinner and longer, they break up into smaller and elliptical drops. The water drop deformation, the breakage rate and, consequently, the water drop size distribution are affected by pump operational conditions. As the impeller rotation and the continuous oil flow rate increase, breakage events become frequent, and the oil drops become smaller due to the associated higher velocities and centrifugal forces. A complete description and visualization of the breakage mechanism are detailed in Perissinotto *et al.* (2020).

Due to these breakage events, small water droplets are always present in the impeller channel. Figure 2 present instantaneous high-speed camera images from the experiments listed in Tab. 1. As observed, independent of the pump operating condition, small water droplets are visible in the image. The size of the small oil drops is in the range of pixels of diameter, with physical diameters ranging from 100 μm to 500 μm, as demonstrated in detail in Fig. 2a). The droplet-based image velocimetry technique, detailed in the next section, is based on the identification and tracking of these small droplets.

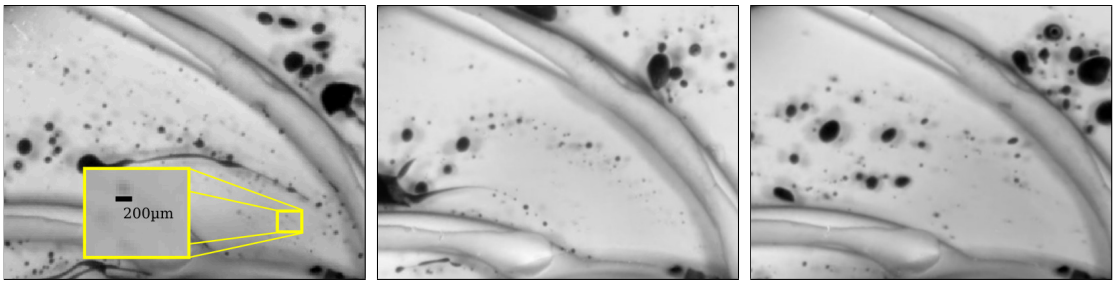

(a) Exp. 1 (b) Exp. 2 (c) Exp. 3

Figure 2: Instantaneous high-speed camera images from the experiments listed in Tab. 1. Independent of pump operating condition, droplets in a range of 100 μm to 500 μm are always present.

3. DROPLET-BASED IMAGE VELOCIMETRY

As described in the previous paragraphs, micro droplets are always present in the flow within the impeller despite the pump's operational conditions. Considering that the continuous phase is viscous (μ_o = 18cP), one can assume that the characteristic time scale of a water droplet τ_{drop} is so small that the droplet can be considered as a fluid tracer particle (Raffel *et al.*, 1998).

In a centrifugal pump, the Coriolis and centrifugal forces play an important role in the flow within the impeller channels. Therefore, the slip velocity between the droplets and the continuous phases must be assessed. The same analysis is necessary when selecting tracer particles in PIV experiments, where the particle diameters and density are of fundamental importance to assure the tracers' ability to follow the fluid streamlines. The criteria is often based on the analysis of a suddenly accelerated particle in a creeping flow, a valid assumption considering the small length of the seeding particles, which usually ranges from 1 to 100 μm (Raffel *et al.*, 1998). For the flow within the pump impeller channels, one must also include the Coriolis and centrifugal forces, as detailed in Choi *et al.* (2004) and Li *et al.* (2016). According to Choi *et al.* (2004), within the impeller channels, the centrifugal term is the dominant force. From a balance between the viscous and centrifugal force, the following relation for the slip velocity U_{slip} is obtained,

$$U_{slip} = U_o - U_w = d_{\mathrm{w}}^2 \frac{(\rho_{\mathrm{w}} - \rho_o)}{18\mu_o} R\,\omega^2, \tag{1}$$

where U is a characteristic velocity of the oil phase U_o and the water droplets U_w, while ω is the impeller rotational speed in rad/s and R is the radius of curvature, which here is defined as the pump impeller outer radius (R = 55 mm).

From Eq. (1), a 100 μm water droplet results in slip velocity of U_{slip} = 1 mm/s, and for 500 μm water droplet, the value is equal to U_{slip} = 27 mm/s. Thus, one can assume that small water droplets acts as tracer particles of the viscous oil phase. The same observation is found when calculating the droplets characteristic time scale, $\tau_{drop} = \rho_o {d_o}^2/18\mu_o$, which is $\tau_{drop} = 0.026$ ms for a 100 μm water droplet and $\tau_{drop} = 0.64$ ms for a 500 μm water droplet.

Despite being visible in the high-speed camera images, additional steps are required to correctly identify the water droplets and track their motion. In the present work, the identification of the water droplets is made by a series of image processing steps, which are centred around the application of an U-Net model (Ronneberger *et al.*, 2015), a convolutional network architecture for precise image segmentation. For this purpose, multiple high-speed camera images were manually labelled to create the training dataset, as depicted in Fig. 3. A total of 23 images in the different pump conditions acquired in Perissinotto *et al.* (2020) were manually labeled to generated the U-Net training and validation dataset.

As observed in this illustration, the original labelled dataset contained all the visible drops in the image, approximated as ellipsoids or, depending on the case, as contours composed of a set of connected points. This labelling followed the same methodology detailed in de Cerqueira *et al.* (2021) for the tracking of oil drops in a centrifugal pump impeller. However, in the present work, to train an U-Net model that only identified the small water droplets, only water drops limited to a diameter of 9 pixels (720μm) were used to generate the labelled masks.

After generating the training and validation dataset, composed of pairs of high-speed camera images and small water droplet masks, the U-Net is model is trained. In order to achieve high-quality segmented images, different U-net architectures were tested through a hyperparameter optimisation analysis (Li *et al.*, 2017). After finishing the training step, the U-Net resulting mask was compared against a validation dataset. Therefore, it was possible to quantify the quality of the masks produced by the U-Net model. A complete description of the U-Net architecture definition and model quality quantification is detailed in de Cerqueira *et al.* (2022), whose methodology is employed in the current work.

Figure 4 shows examples of the segmented images, where it is visible that the U-Net is only masking the small water droplets, ignoring the other water drops. For instance, in Fig. 4c), the U-Net is detecting the small water droplets generated due to thinning and, subsequent breakage, of a large deformed water drop. At first glance, it seems unnecessary to employ such sophisticated image processing to detect the contours of dark-dyed drops flowing in a bright white background.

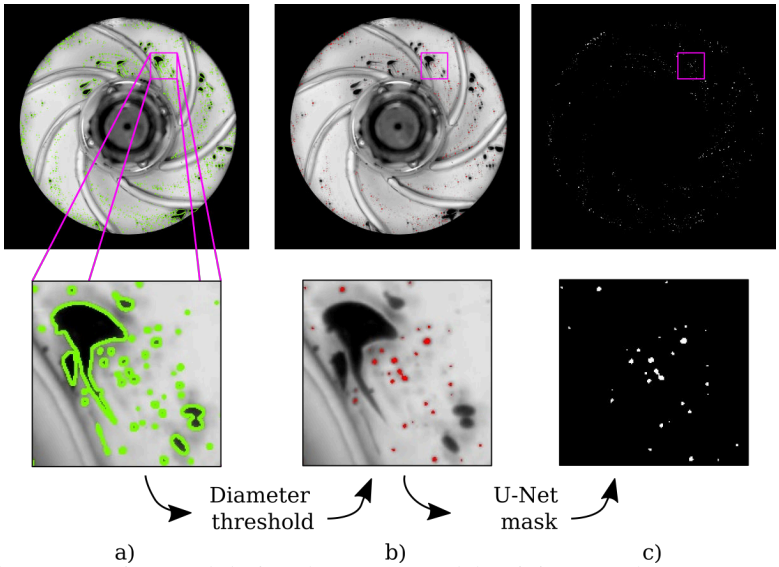

Figure 3: Example of dataset creation used during the U-Net model training: a) The green contours on the raw images represent the manually created contours; b) From the originally labelled water drops, only water droplets with diameter of less than 9 pixels were used to produce the U-Net mask; c) U-Net mask with only the small water droplets.

However, due to the direct illumination setup adopted in Perissinotto *et al.* (2020), as the impeller rotates around its axis, multiple shadows are cast into the image, difficulting the small water drops detection by traditional techniques, such as the use of Canny (Canny, 1986) algorithm as used by Ziegenhein *et al.* (2016) to identify microbubbles in shadowgraphy images.

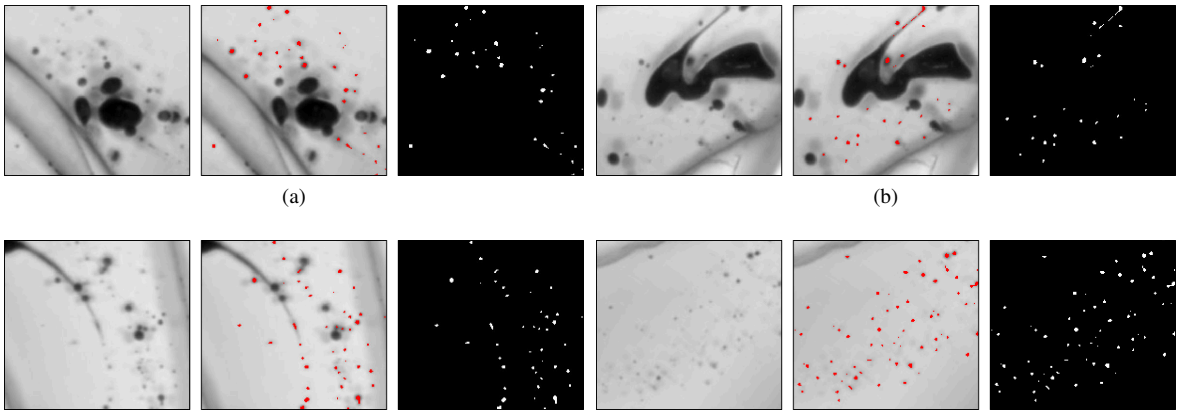

Figure 4: Detail of the image segmentation masks produced by the U-Net model, presenting the raw HSC images (left pane), highlighted drops (middle pane) from the U-Net mask (right pane).

From the U-Net segmented images, the continuous oil velocity field, under the assumptions listed in the current work, can be estimated through the PIV or the PTV technique. In the current work, we opted to use the PTV algorithm described in de Cerqueira *et al.* (2021) and de Cerqueira *et al.* (2022) to compute the water droplets' instantaneous velocity. Since the images were acquired at a 2000 fps acquisition rate, the temporal spacing between two frames is set Δt= 500 μs to convert the PTV pixel displacement to physical velocities. The PTV returns the velocity from each water droplet in a Lagrangian frame of reference. In order to evaluate the flow field, the variables are mapped back to a fixed Eulerian background mesh, following the methodology adopted in Cerqueira and Paladino (2021) and de Cerqueira *et al.* (2022). At this point, it is important to state that the PIV technique and also some PTV applications are based on planar images from a thin illumination sheet. That is not the case in the current work, where the transparent pump impeller prototype is volumetric illuminated. However, since the pump impeller height is small, h= 6mm, the results presented here return a representative picture of the flow structure within the pump impeller.

4. RESULTS AND DISCUSSIONS

4.1 Assessment o the droplet-based image velocimetry

Before analyzing the flow within the pump impeller's channels at the three different conditions listed in Tab. 1, the ensemble-averaged oil flow rate is compared against the experimental values from the Coriolis flowmeter installed in the experimental setup. In order to verify the assumption that the small water droplets acted as tracer particles, the mass flow rate $\dot{m}_o^{PTV}$ was calculated with six different droplet size group, with droplets sizes ranging into: i) 0 – 100 μm; ii) 100 – 200 μm; iii) 200 – 300 μm, iv) 300 – 400 μm and v) 400 – 500 μm. The $\dot{m}_o^{PTV}(r)$ was calculated in different r circumferential cross sections from the impeller center as,

$$\dot{m}_o^{PTV}(r) = \int_{S(r)} \rho_o \langle \vec{u}_{PTV,i}(r) \rangle \cdot \hat{n}\, dS \tag{2}$$

where $\langle \vec{u}_{PTV,i}(r) \rangle$ is the averaged PTV velocity at the circumferential plane $S(r)$ located r distance away from the impeller center, while $\hat{n}$ is the outward pointing normal vector and dS(=$r\, dr\, h$) the differential surface element.

The mass flow rate at different sections of the pump impeller channel sections for each droplet size is shown in Fig. 5 for Exp. 3 from Tab. 1, the flow condition with higher $\dot{m}_o$ from our experimental matrix.

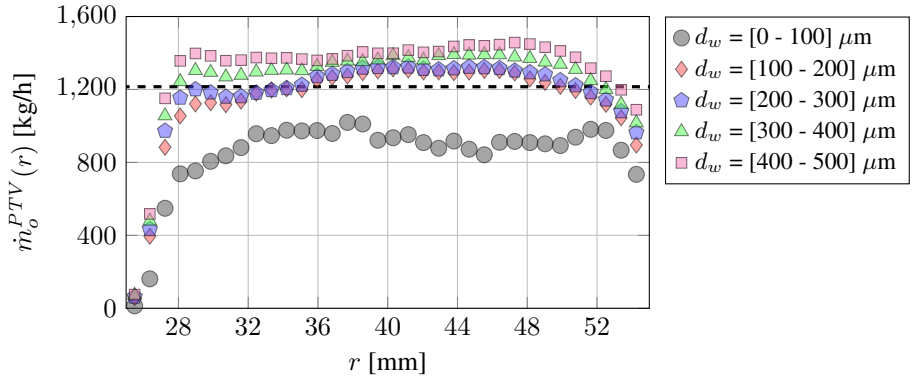

Figure 5: Calculated mass flow rate at different impeller pump sections from different water droplet sizes. The dashed line represents the experimentally measured value $\dot{m}_o$ by the Coriolis flowmeter for Exp. 3 of Tab. 1.

As observed, the computed $\dot{m}_o$ are not resulting in a constant value, as would be expected due to mass continuity constraint. This is the result of a combination of two major factors. The first is that the measured values represent average velocity along the pump impeller channels height direction (h = 6mm). Therefore, if the water droplets are acting as tracer particles, the $\dot{m}_o^{PTV}(r)$ should result in values close to the expected mass flow rate measured by the Coriolis flowmeter only in certain cases. Due to the high viscous fluid, a velocity profile between the classical parabolic laminar and flat turbulent profile in the z-direction is expected. In addition, in centrifugal pumps and other rotating fluid machinery, the Coriolis acceleration may induce secondary flows (Gülich, 2008), resulting in complex velocity profiles. In summary, if the velocity profile is close to the flat velocity profile, Eq. (2) should result in mass flow rates close to the ones acquired by the Coriolis flowmeter. The opposite may indicate complex velocity profiles, such as close to the pump impeller channel inlet sections, where the fluid acceleration is stronger, and the flow may be affected by swirl prior to entering the channels. The same issue is found when estimating the mass flow rate from planar PIV results (Perissinotto, 2022). The second discrepancy is associated with the experimental uncertainties of the Coriolis flowmeter and the ensemble-averaged PTV velocity results. Nonetheless, the $\dot{m}_o^{PTV}(r)$ values for water-droplets with a maximum diameter of 300 μm presents a good agreement with the measured Coriolis mass flow rate.

Figure 6 shows the ensemble-averaged PTV results from for Exp. 3 listed in Tab. 1 for the first four water droplets classes size from Fig. 5. For better illustration purposes, Fig. 6 presents only a quadrant of the entire ensemble-average velocity results. In addition, the results from Fig. 6 and the following two-dimensional velocity vector fields are presented in a rotating frame of reference attached to the pump impeller.

The velocity fields from Fig. 6 from the different water droplet sizes present similar flow patterns. Due to the small occurrence and also the difficulties in tracking and identifying the smaller droplets, not enough droplets are found in the 0-100 μm range. For instance, close to the impeller blades, the illumination setup may cause shadows closer to its edges, and the small water droplets may not be identified in this region. That is the exact reason why for the 0-100 μm range, there is a lack of velocity vectors close to the impeller blades in Fig. 6. This explain the reduced values of $\dot{m}_o^{PTV}(r)$ in the curves shown in Fig. 6. The velocity distributions are similar for the remaining cases, with slightly higher values for the larger water droplets within the 300-400 μm range.

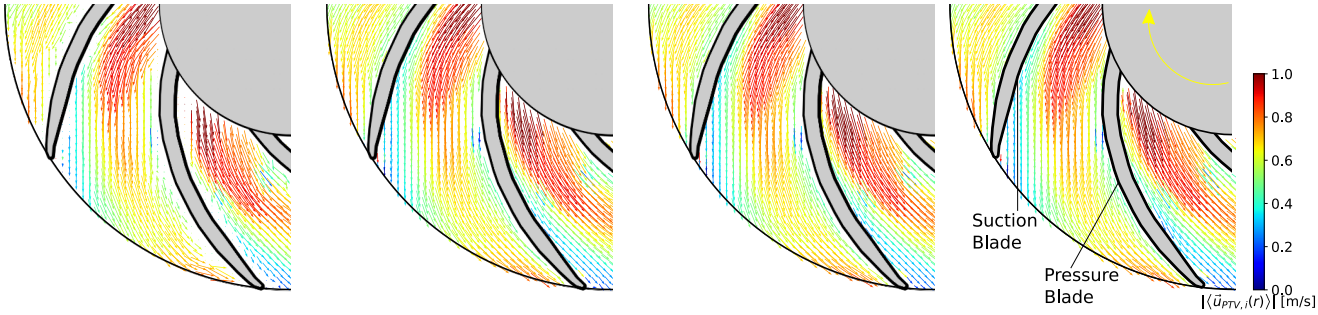

(a) d_w = [0 - 100] μm (b) d_w = [100 - 200] μm (c) d_w = [200 - 300] μm (d) d_w = [300 - 400] μm

Figure 6: Ensemble-average PTV velocity fields from Exp. 3 for different water droplets classes. The yellow clockwise arrow in d) indicates impeller rotational direction.

The same trends, resulting in the same conclusions, are found when analyzing the other cases listed in Tab. 1. From the results and discussions from this section, it is possible to affirm that the velocity fields from water droplets in the 0-300 μm range represent the velocity vectors of the continuous, viscous oil phase. Therefore, the PTV results from droplets in the 0-300 μm range are going to be used to analyze the flow within the pump impeller in the subsequent paragraphs.

4.2 Ensemble-average velocity fields

Figure 7 presents the ensemble-average PTV results from the 0-300 μm range water droplets in the three pump operating conditions listed in Tab. 1.

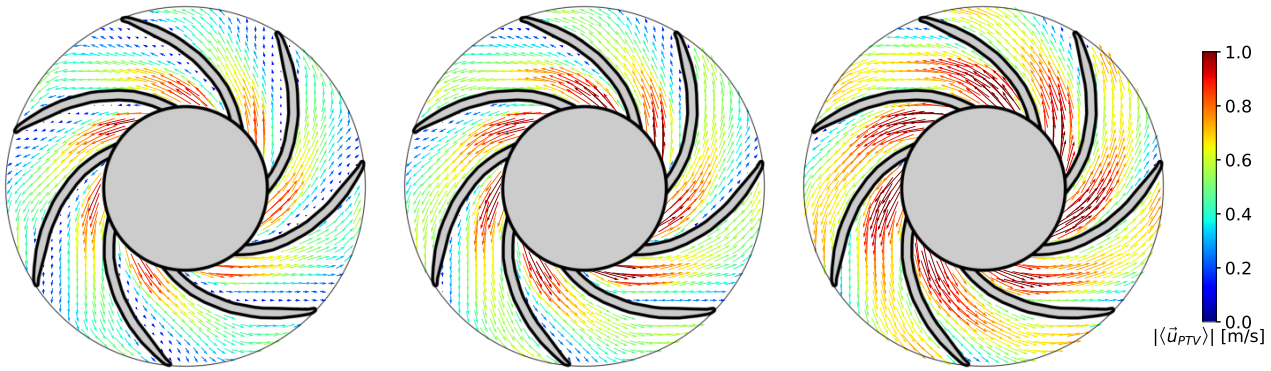

(a) Exp. 1 - $Q_o = 0.8\,Q_{BEP}$ (b) Exp. 2 - $Q_o = 1.0\,Q_{BEP}$ (c) Exp. 3 - $Q_o = 1.2\,Q_{BEP}$

Figure 7: Ensemble-average PTV velocity fields for the three pump operating conditions listed in Tab. 1. For better visualization of the flow structure, the spatial resolution is reduced.

As expected, the effect of the flow rate is visible on the vector velocity fields from Fig. 7, with the velocity magnitude increasing with the Q_{BEP} value. For the $Q_o = 0.8\,Q_{BEP}$ case, low velocity regions are observed close to the suction blade, and the velocity vectors are not aligned with the impeller blades. As the mass flow rate increases, reaching the BEP ($Q_o = 1.0\,Q_{BEP}$), the low velocity region close to the suction blades is reduced and the flow follows the impeller blade curvature smoothly. For a mass flow rate above the BEP, ($Q_o = 1.2\,Q_{BEP}$), the low velocity region close to the suction blade is only visible close to the pump impeller outlet section, while the flow is aligned with the blade geometry. A similar result is found in the PIV results from Li *et al.* (2020).

Before continuing into the analysis of the turbulent statistics, it is important to point out that in the current configuration, the tracer particle seeding is not controlled in the present experiments, but occurs naturally due to the breakage of the water droplets. Therefore, we cannot assure that the PTV results are not biased due to this non-uniform injection, despite similarity with the results from Li *et al.* (2020). The second point is that the results are ensemble-averaged, which is not ideal in this case since the pump prototype presented a (not transparent) vaned diffuser located after the impeller channel outlet. Ideally, those results should be phase-averaged, i.e., averaged in equal impeller angle positions, to better observe the effect of the diffuser on the flow pattern within the impeller channels. Nonetheless, the results presented here are solid and represent the flow structure, and as shown in the next section, capture the influence of the diffuser on the velocity fields within the impeller channels.

4.3 Turbulent Statistics

The turbulent kinetic energy TKE fields are shown in Fig. 8, where

$$TKE = \frac{1}{2}\left[\left\langle (u_{PTV}{}')^2 \right\rangle + \left\langle (v_{PTV}{}')^2 \right\rangle\right] \tag{3}$$

where $u_{PTV}{}'$ and $v_{PTV}{}'$ are the velocity fluctuations from the u and v velocity components. As in the result of Fig. 7, the distribution from Fig. 8 shows that due to small imperfections of the pump impeller prototype geometry and construction, small deviations are found in the flow within the impeller channels. However, the flow pattern is similar within the different channels.

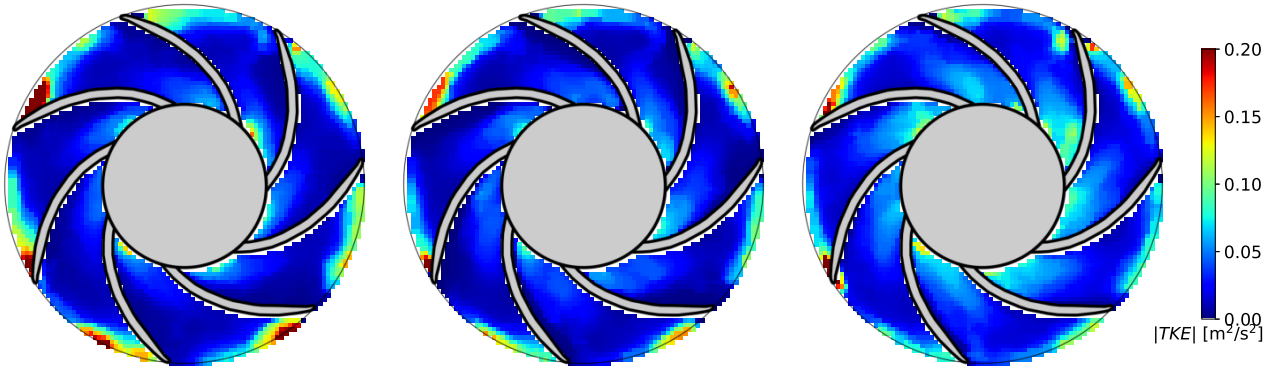

(a) Exp. 1 - $Q_o = 0.8\,Q_{BEP}$ (b) Exp. 2 - $Q_o = 1.0\,Q_{BEP}$ (c) Exp. 3 - $Q_o = 1.2\,Q_{BEP}$

Figure 8: Turbulent kinetic energy TKE fields for the three pump operating conditions listed in Tab. 1.

The turbulent kinetic energy fields from Fig. 8 present a similar distribution throughout the entire domain, presenting higher values close to the impeller channel inlet and outlet sections. The higher values can be a result of the sudden change in the direction as the fluid leaves the inlet diffuser and enters the impeller channels. At the inlet section, the local TKE values increase with the flow rate due to the associated higher fluid velocities. The same increase in the TKE field is observed in the central regions of the impeller channel, again, due to the associated higher fluid velocities. At the outlet section, it is possible to observe the influence of the outlet vaned diffuser on the flow within the impeller channels, where TKE peaks are present close to the pressure section over the three tested pump operational conditions. The same turbulent kinetic energy distribution is observed in the work of Feng *et al.* (2010) close to the outlet section, which studied the flow within the region between the impeller and vaned diffuser through the Laser Doppler Velocimetry (LDV) technique. Still, in this region, as opposed to what is found throughout the domain, the TKE values decrease as the oil flow rate is reduced. The same observation is described in Feng *et al.* (2010), where the working fluid was water, a less viscous fluid than the mineral oil used in the present work.

Figure 9 shows a sequence of frames where it is possible to observe the influence of the outlet diffuser at the outlet section. The snapshots of Fig. 9 were taken from a high-speed camera acquisition of $Q_o = 0.8\,Q_{BEP}$, but the flow pattern is observed in the remaining cases. While leaving the impeller channel, the small water drops exit the section in a counter-clockwise vortical motion close to the pressure blade. For a given channel, when the suction blade tip passes close to a stationary diffuser blade, the fluid faces a strong deceleration and a sudden change of direction while exiting the impeller, shedding a small vortex, visible in the image sequence of Fig. 9.

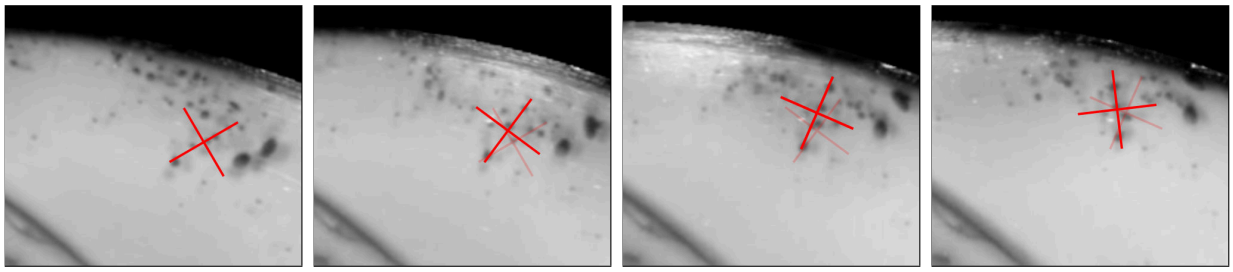

(a) t = 0.0 ms (b) t = 2.5 ms (c) t = 5.0 ms (d) t = 7.5 ms

Figure 9: Sequence of image frames close to the pump impeller outlet section, highlighting the counter-clockwise vortical motion of the water droplets near the pressure blade.

By comparing the snapshots from Fig. 9 with the turbulent kinetic energy field distribution from Fig. 8, it is possible to understand the reason TKE decreases with an increase of the average flow velocity. At Q_o = $0.8\,Q_{BEP}$, the vortex shed from the suction blade tip slowly travels out of the impeller channel, promoting the turbulence close to the impeller outlet. As the flow rate increases, Q_o = $1.0\,Q_{BEP}$, as the vortex is formed, it quickly travels out of the channel due to the higher surrounding fluid velocities, therefore, reducing the local turbulent kinetic fields. This also explains the reason why a further reduction of the local TKE distribution is observed in the Q_o = $1.2\,Q_{BEP}$ case, where the vortex travels out of the impeller channel even faster.

5. CONCLUSIONS

The current work presents the development of a droplet-based velocimetry technique applied to two-phase water-oil dispersion flows. The technique is applied to the high-speed camera images from Perissinotto *et al.* (2020), which performed a flow visualization study on water-in-oil dispersion flow in a centrifugal pump impeller. In the experiments, small water droplets naturally occurred during injection into the pump impeller channel and due breakage events. The occurrence of small water droplets, with a maximum size of 500 μm, in combination with the viscous continuous oil phase (μ_o = 18.0 cP), meant that those droplets could be assumed as tracer particles from the continuous phase. According to simple dynamic relations found in the literature, despite the intense centrifugal acceleration common to rotodynamic machines, the slip for dispersed droplets with a maximum diameter of 500 μm is negligible.

By using a set of image processing techniques, it was possible to identify the small water droplets and group them into different size intervals. Then, the instantaneous velocity of the small water droplets was calculated through the PTV technique. In order to assess the velocimetry technique described in this paper, the mass flow rate is calculated from the ensemble-average PTV results and compared against the experimentally measured values from the Coriolis meter. The comparison shows that water droplets smaller than 300 μm can be used as tracer particles from the continuous, viscous oil phase.

After the assessment study, the technique is applied to estimate the ensemble-average velocity field and turbulent statistics in three pump operational conditions ($Q_o = [0.8, 1.0, 1.2]Q_{BEP}$) with a fixed impeller rotational speed (N = 600 rpm). The flow structure of the different acquisitions obtained here agrees with PIV and LDV studies' results found in the literature for centrifugal pump impellers, demonstrating that, although there are a few limitations compared to the PIV technique, the technique here described can be seen as a cheap alternative for estimating multi-dimensional velocity fields in two-phase dispersions.

The results presented here demonstrate that the technique can be adapted for single-phase internal flows in complex geometries, where the PIV is prohibitive due to difficulties associated with the planar illumination or in multiphase flow situations, where the same illumination issues are present. For these cases, small dispersed droplets or even common PIV tracer particles could be added to the flow, and by carefully controlling the camera depth of field and focus Ziegenhein *et al.* (2016), one could estimate the velocity field in these situations.

6. ACKNOWLEDGEMENTS

We gratefully acknowledge the support of EPIC - Energy Production Innovation Center, hosted by the University of Campinas (UNICAMP) and sponsored by Equinor Brazil and FAPESP – Sao Paulo Research Foundation (Process Number 2017/15736-3). We also thank FAPESP for providing the PIV system used in this study through the Multi-User Equipment program (Process Number 2019/20870-6). We acknowledge the support of ANP (Brazil's National Oil, Natural Gas and Biofuels Agency) through the R&D levy regulation. The acknowledgments are also extended to Center for Petroleum Studies (CEPETRO), School of Mechanical Engineering (FEM), and ALFA Research Group.

7. REFERENCES

Bulgarelli, N.A.V., Biazussi, J.L., Monte Verde, W., Perles, C.E., de Castro, M.S. and Bannwart, A.C., 2021. "Experimental investigation on the performance of Electrical Submersible Pump (ESP) operating with unstable water/oil emulsions". *Journal of Petroleum Science and Engineering*, Vol. 197, No. September 2020, p. 107900. ISSN 09204105.

Canny, J., 1986. "A computational approach to edge detection". *IEEE Transactions on pattern analysis and machine intelligence*, , No. 6, pp. 679–698.

Cerqueira, R.F. and Paladino, E.E., 2021. "Development of a deep learning-based image processing technique for bubble pattern recognition and shape reconstruction in dense bubbly flows". *Chemical Engineering Science*, Vol. 230, p. 116163.

Cerqueira, R., Paladino, E., Ynumaru, B. and Maliska, C., 2018. "Image processing techniques for the measurement of two-phase bubbly pipe flows using particle image and tracking velocimetry (piv/ptv)". *Chemical Engineering Science*, Vol. 189, pp. 1–23.

Choi, Y.D., Nishino, K., Kurokawa, J. and Matsui, J., 2004. "Piv measurement of internal flow characteristics of very low

specific speed semi-open impeller". *Experiments in Fluids*, Vol. 37, pp. 617–630. ISSN 0723-4864.

de Cerqueira, R.F.L., Perissinotto, R., Verde, W.M., Biazussi, J.L., de Castro, M.S. and Bannwart, A., 2021. "Development of a particle tracking velocimetry (PTV) measurement technique for the experimental investigation of oil drops behavior in dispersed oil-water two-phase flow within a centrifugal pump impeller". In *Proceedings of the 26th International Congress of Mechanical Engineering*. ABCM.

de Cerqueira, R.F.L., Perissinotto, R., Verde, W.M., Biazussi, J.L., de Castro, M.S. and Bannwart, A., 2022. "Development and assessment of a particle tracking velocimetry (ptv) measurement technique for the experimental investigation of oil drops behavior in dispersed oil-water two-phase flow within a centrifugal pump impeller". Unpublished work.

Feng, J., Benra, F.K. and Dohmen, H.J., 2010. "Investigation of periodically unsteady flow in a radial pump by CFD simulations and LDV measurements". *Journal of Turbomachinery*, Vol. 133, No. 1.

Gülich, J.F., 2008. *Centrifugal pumps*, Vol. 2. Springer.

Keller, J., Blanco, E., Barrio, R. and Parrondo, J., 2014. "Piv measurements of the unsteady flow structures in a volute centrifugal pump at a high flow rate". *Experiments in fluids*, Vol. 55, No. 10, pp. 1–14.

Li, L., Jamieson, K., DeSalvo, G., Rostamizadeh, A. and Talwalkar, A., 2017. "Hyperband: A novel bandit-based approach to hyperparameter optimization". *The Journal of Machine Learning Research*, Vol. 18, No. 1, pp. 6765–6816.

Li, X., Chen, B., Luo, X. and Zhu, Z., 2020. "Effects of flow pattern on hydraulic performance and energy conversion characterisation in a centrifugal pump". *Renewable Energy*, Vol. 151, pp. 475–487.

Li, Y., Yuan, S., Wang, X., Tan, S.K. and Mao, J., 2016. "Comparison of flow fields in a centrifugal pump among different tracer particles by particle image velocimetry". *Journal of Fluids Engineering*, Vol. 138. ISSN 0098-2202.

Liu, X.D., Liu, Z.Q., Zhong, Q., Li, Y.j. and Yang, W., 2021. "Experimental investigation of relative velocity field based on image rotation method in pump impeller". *Flow Measurement and Instrumentation*, Vol. 82, p. 102061.

Monte Verde, W., Biazussi, J., Bannwart, A., Sassim, N.A. and Estevam, V., 2013. "Gas and viscous effects on the esps performance". In *SPE Artificial Lift Conference-Americas*. OnePetro.

Monte Verde, W., Biazussi, J.L., Sassim, N.A. and Bannwart, A.C., 2017. "Experimental study of gas-liquid two-phase flow patterns within centrifugal pumps impellers". *Experimental Thermal and Fluid Science*, Vol. 85, pp. 37–51. ISSN 08941777.

Perissinotto, R., 2022. *Estudo Experimental de Visualização de Escoamentos no Interior de Impelidores de Bombas Centrífugas*. Ph.D. thesis, University of Campinas - UNICAMP.

Perissinotto, R.M., Monte Verde, W., Biazussi, J.L., Bulgarelli, N.A.V., Fonseca, W.D.P., de Castro, M.S., Franklin, E.d.M. and Bannwart, A.C., 2021. "Flow visualization in centrifugal pumps: A review of methods and experimental studies". *Journal of Petroleum Science and Engineering*, Vol. 203, No. January, p. 108582. ISSN 09204105.

Perissinotto, R.M., Monte Verde, W., de Castro, M.S., Biazussi, J.L., Estevam, V. and Bannwart, A.C., 2019. "Experimental investigation of oil drops behavior in dispersed oil-water two-phase flow within a centrifugal pump impeller". *Experimental Thermal and Fluid Science*, Vol. 105, No. November 2018, pp. 11–26. ISSN 08941777.

Perissinotto, R.M., Monte Verde, W., Perles, C.E., Biazussi, J.L., de Castro, M.S. and Bannwart, A.C., 2020. "Experimental analysis on the behavior of water drops dispersed in oil within a centrifugal pump impeller". *Experimental Thermal and Fluid Science*, Vol. 112, No. November 2019, p. 109969. ISSN 08941777.

Raffel, M., Willert, C.E., Kompenhans, J. *et al.*, 1998. *Particle image velocimetry: a practical guide*, Vol. 2. Springer.

Ronneberger, O., Fischer, P. and Brox, T., 2015. "U-net: Convolutional networks for biomedical image segmentation". In *International Conference on Medical image computing and computer-assisted intervention*. Springer, pp. 234–241.

Stel, H., Ofuchi, E.M., Sabino, R.H., Ancajima, F.C., Bertoldi, D., Marcelino Neto, M.A. and Morales, R.E., 2019. "Investigation of the motion of bubbles in a centrifugal pump impeller". *Journal of Fluids Engineering, Transactions of the ASME*, Vol. 141, No. 3, pp. 1–14. ISSN 1528901X.

Zhang, J., Cai, S., Li, Y., Zhu, H. and Zhang, Y., 2016. "Visualization study of gas-liquid two-phase flow patterns inside a three-stage rotodynamic multiphase pump". *Experimental Thermal and Fluid Science*, Vol. 70, pp. 125–138. ISSN 08941777.

Zhao, L., Chang, Z., Zhang, Z., Huang, R. and He, D., 2021. "Visualization of gas-liquid flow pattern in a centrifugal pump impeller and its influence on the pump performance". *Measurement: Sensors*, Vol. 13, No. November 2020, p. 100033. ISSN 26659174.

Ziegenhein, T., Garcon, M. and Lucas, D., 2016. "Particle tracking using micro bubbles in bubbly flows". *Chemical Engineering Science*, Vol. 153, pp. 155–164.

8. RESPONSIBILITY NOTICE

The authors are solely responsible for the printed material included in this paper.